Dalton Transactions

Accepted Manuscript

ROYAL SOCIETY OF CHEMISTRY

www.rsc.org/dalton

Analysis of the influence of synthetic paramaters on the structure and physico-chemical properties of non-spherical iron oxide nanocrystals and their biological stability and compatibility.

Alberto Pardo,[a] Rosa Pujales,[a] Mateo Blanco,[a] Eva M. Villar-Alvarez,[a] Silvia Barbosa,[*a] Pablo Taboada,[*a] Víctor Mosquera[a]

[a]*Grupo de Física de Coloides y Polímeros, Departamento de Física de la Materia Condensada; 15782-Santiago de Compostela, Spain*

To whom correspondence should be addressed: silvia.barbosa@usc.es; pablo.taboada@usc.es

Abstract

In this work, we analyzed the effect of subtle changes in the syntehtic conditions and synthetic parameters on the resulting size, shape, monodispersity, crystallinity and magnetic properties of iron oxide nanocrystals (IONCs) obtained through a modified one pot method for the production of mainly cubic-shaped nanoparticles (NPs). Cubic, octahedral and cuboctahedral shapes with different sizes and monodispersity could be obtained by slightly changing the stabilizer/precursor molar ratio, the precursor concentration, the reaction time and temperature and/or the heating rate. Their physical properties were evaluated using high-resolution trasmission electron microscopy (HRTEM), X-ray powder diffraction (XRD), selected-area electron diffraction (SAED) and a superconducting quantum interference (SQUID) device. It was found that monodisperse cubic nanocrystals from ca. 25 to 94 nm could be obtained either by changing the precursor concentration, the heating rate or the reaction time. These cubic nanocrystals were ferrimagnetic in the whole temperature rage analyzed, with saturation magnetization values even larger than those of bulk magnetite. In addition, slightly truncated octahedral NPs could be achieved at relatively large heating ramp rates, whereas cubooctahedral NPs were derived by simply increasing the stabilizer/precursor molar ratio. Saturation magnetization of both types of NPs were slightly lower than cubic ones, but they were still ferrimagnetic in the whole temperature range analyzed. Moreover, transfer to aqueous solution was possible by a ligand exchange with dimercaptosuccinic acid (DMSA) providing, at the same time, chemical groups for additional functionalization if required. The DMSA-coated cubic IONCs were fairly stable in culture medium, allowing their internalization by different cell types. The NPs inside the cells were located in the cytoplams and most of them showed a perinuclear distribution.

Moreover, a great cytocompatibility in a large range of particle concentrations was observed without induction of morphological changes in the cultured cells.

KEYWORDS: Iron oxide nanocrystals, shape control, ferrimagnetism, colloidal stability, cytocompatibility.

1. Introduction

Magnetic characteristics are crucial for the successful performance of nanoparticles (NPs) such as contrast agents in magnetic resonance imaging (MRI), nanoplatforms and supports for magnetic guiadance in drug delivery, magnetic separation, cellular signaling, and as heat mediators in hyperthermia treatments.[1-5] Among the different materials that have shown promising magnetic properties (high saturation magnetization, relatively moderate anisotropy constant K_{eff}, and high initial susceptibility),[6] iron oxide nanocrystals (IONCs) are by far the most studied ones also because of their biocompatibility and availability. IONCs indeed can be prepared by simple methods, like co-precipitation or sol-gel techniques in large batches, but the resulting nanoparticles (NPs) usually show a considerable polydispersity,[7-8] which could compromise their magnetic behavior and absorptivity properties. Additionally, despite ferri- or ferromagnetic NPs are desiderable for many of the former applications, superparamagnetic IONCs of <30 nm have generally been used because scarce preparation methods are available for the synthesis of uniform ferrimagnetic NPs larger than 20-30 nm. Interestingly, in nature magnetotactic bacteria[9] can produce single-domain monodisperse IONCs of magnetite type in the size range 20-100 nm with a faceted cubic or cubooctahedric shape enwrapped within a membrane bilayer, the so-called “magnetosomes”, exhibiting high saturation magnetization and

crystallinity and elevated specific absorption rate (SAR) values.[10] In order to obtain in laboratory such monodisperse cubic magnetic structures a recent approach is represented by thermal decompositon methods, in which an iron organometallic precursor, such as iron pertacarbonyl ($FeCO_5$), iron(II) and iron(III) acetylacetonates ($Fe(acac)_2$ and $Fe(acac)_3$, respectively), or an iron-oleate complex, is decomposed in a high boiling organic solvent.[3,11] The different components within the reaction mixture and the various chemical reactions that can occur involving the organic components present in the reaction medium during the preparation of these cubic IONCs play a key role on the control of their, size, shape and monodispersity. Hyeon *et al.* showed that with changes in the iron precursor concentration magnetic iron oxide nanocubes of sizes ranging from ca. 20 to 60 nm can be obtained in an one-pot synthetic process using oleic acid (OA) as stabilizing agent and benzyl ether as the organic solvent.[12] These authors also showed that by increasing the reaction time while diminishing the volume of organic solvent a controlled size increase of the faceted MNPs could be also obtained up to 150 nm, while also allowing to control the NP morphology from truncated cube and truncated octahedra to perfect cubic morphologies, respectively.[13] Cheon *et al.* have also shown[12] that the size of cubic zinc-ferrite nanocrystals can be tuned from 20 to 160 nm by simply changing the metallic precursor concentration.[14] By careful control of the heating rate ramp, Guardia *et al.* could also obtain magnetic nanocubes with sizes ranging from 45 to 180 nm through a similar synthetic process, but changing OA by decanoic acid as the stabilizing agent.[15] In a later study, the nanocube sizes could be additionally decreased by modifications in the degassing step prior thermal decomposition.[16] Zhang *et al.* have also shown that cubic cobalt-ferrite iron oxide nanocubes ($CoFe_2O_4$) of sizes between 8 and 11 nm could be obtained by the thermal decomposition of $Fe(acac)_3$ and $Co(acac)_2$ in a mixture of phenyl ehter,

OA, oleylamine and 1,2-hexadecanediol using a seed-mediated growth approach by careful control of the reaction temperature and seed size.[17] Heiss *et al.* have also shown that cubic IONCs of 9-23 nm could be obtained in the presence of sodium oleate as stabilizer by changing the composition of the organic solvent mixture to adjust the reflux temperatures in the range 290-375 ºC.[18]

In spite of the great effort made to control the obtention of cubic IONCs, systematic studies analyzing and fully reporting in detail the influence of less restrictive syntehtic conditions and of different synthetic parameters on the size, shape and magnetic properties of the resulting IONCs are still largely lacking. Hence, in the present work we present the controlled obtention of several IONCs with different shapes as cubes, octahedra and cubooctahedra with tunable sizes by means of an one-pot decomposition route[13] with modifications, in particular under less stringent environmental conditions, and systematically analyzing the effect of different synthesis parameters (precursor concentration, stabilizer/precursor mole ratio, heating rate, reaction time or reaction temperature) on the size, shape, crystallinity and magnetic properties of the resulting magnetic IONCs. In this manner, we were able to obtained cubic IONCs of different sizes from 28 to 94 nm, but also truncated octahedral and cubooctahedral IONCs by, for example, only changing the heating rate ramp or the precursor/stabilizer molar ratio, respectively. The magnetic analysis showed that all obtained IONCs are in a ferrimagnetic state in the whole temperature range analyzed, with a blocking temperature above 300 K. Moreover, nanocubes displayed saturation magnetizations even larger than that of bulk magnetite and a similar magnetic anisotropy than bulk Fe at low temperature. To exploit the potential used of this type of NPs as imaging probes and/or therapeutic platform, the cellular uptake and toxicity response of cubic IONCs were also analyzed. Beforehand,

aqueous solubility to cubic IONCs was provided through a ligand exchange process using dimercaptosuccinic acid (DMSA) as the coating material. The DMSA-coated IONCs were proved to be fairly stable in aqueous and culture medium conditions, allowing further post-functionalization. In addition, these NPs were well internalized by different cell types and located within the cytoplasm, showing a perinuclear arrangement at most, without inducing significant toxical effects in a wide range of concentrations. Hence, this type of particles would be of potential use as cores/substrates to design new multifunctional nanoplatforms for combined therapeutic and/or diagnostic capabilities.

2. Materials and methods

2.1 Materials

Iron(III) acetylacetonate (99%), oleic acid (99%) and dibenzyl ether (99%) were purchaed from Sigma Aldrich Co. MDA-MB-231 adenocarcinoma breast, HeLa cervical cancer cells and msenchemycal stem cells (MSC) from Cell Biolabs (San Diego, CA, USA) were used for *in vitro* studies. Dulbecco's Modified Eagle Medium (DMEM), fetal bovine serum (FBS), L-glutamine, penicillin/streptomycin, sodium pyruvate, and MEM Non-Essential Amino Acids (NEAA) were from Invitrogen. All solvents used were of analytical grade and were also purchased from Sigma-Aldrich. All chemicals were used as received.

2.2 Synthesis of IONCS

All experiments were carried out in a standard Schlenk line using 250 mL four-neck round-bottom flasks connected to water-cooled condensers. In a typical

synthesis for iron oxide nanocubes, 0.706 g of $Fe(acac)_3$ (2 mmol) was mixed with 1.4 g of OA (4 mmol) in 10 mL of benzyl ether. The solution was subjected to N_2 flow for 1 h, next heated to reflux at 290 ºC at a rate of 3ºC/min and kept for 30 min at this temperature. No significant changes were found when subjecting the sample solution to a degassing process of 1 h prior the synthesis in terms of yield, size and monodispersity of the samples. However, the controlled presence of oxygen in the reaction vessel led to smaller and slightly more polydisperse cubic NPs (not shown). After cooling to room temperature, 50 mL of a 20/80 (v/v) hexane/toluene mixture was added and the whole solution was centrifuged at 5000 rpm. After removing the supernatant, the black precipitate was redispersed in 2-3 mL of propanol and the washing procedure was repeated at least two more times in similar conditions. Finally, collected particles of size ca. 48 nm were dispersed in 10 mL of hexane. Iron oxide NPs of other sizes were obtained by varying the precursor concentration, the heating rate, the reaction time, or the degassing step. In particular, it has to be remarked that the absence of a degassing step also led to the formation of highly uniform cubic nanocrystals in high yield and with similar sizes than those obtained when vacuum was applied. Moreover, other NP geometries as cubooctahedra and octahedra were also obtained by modifications in the stabilizer/precursor molar ratio, the heating rate or the reaction temperature.

2.3 Characterization of IONCs

To characterize the size and shape of the obtained IONCs TEM images were obtained with a transmission electron microscope (Phillips CM-12) operating at an accelerating voltage of 120 kV as previously described. HR-TEM images and SAED patterns were obtained with a transmission electron microscope (Carl-Zeiss Libra 200

FE-EFTEM) operating at 200 kV. Electron diffraction X-ray spectroscopy (EDX) was performed using a FESEM ultra Plus electronic microscopes operating at 20 kV. Samples were prepared for analysis by evaporating a drop of the hybrid NP dispersion on a carbon coated copper grid without staining (TEM). X-ray diffraction experiments were carried out with a rotating anode X-ray generator (Siemens D5005). Twin Göbel mirrors were used to produce a well-collimated beam of Cu Kα radiation (λ = 1.5418 Å). X-ray diffraction patterns were recorded with an imaging plate detector (AXS F.Nr. J2–394). Iron concentrations of each sample for SQUID were determined by inductively coupled plasma mass spectrometry (ICP-MS) in a Varian 820-MS equipment (Agilent Technologies). On the other hand, magnetic characterization of IONCs were carried out with a SQUID magnetometer (Quantum Design MPMS5, San Diego, CA). Magnetization curves were measured from -50000 to 50000 Oe at different temperatures upon zero field cooling (ZFC) and field cooling (FC) conditions.

2.4. Aqueous solubility and stability of IONCs

To impart water stability, the IONCs was surface-functionalized with DMSA. For the DMSA functionalization, IONCs were coagulated from the hexane suspension by adding ethanol and centrifuging. A mixture of 12 mL of toluene and a solution of 45 mg of DMSA in 2.5 mL of dimethyl sulfoxide (DMSO) was added to 25 mg of IONCs. The mixture was sonicated for 10 min in an ice bath and mechanically stirred during 24 h at room temperature. The DMSA-functionalized NP was washed several times with ethanol, and re-dispersed in water. The pH of aqueous suspension was increased to 10 with 1 M KOH solution, to deprotonate one of the DMSA carboxylic groups and thiol groups (pK 9.2), to achieve a better dispersion. Then, pH was

brought back to pH 7 with a 1 MHNO_3 solution and the NP solution dualyzed for 2 days. The successful formation of the DMSA-coating layer was analyzed by Fourier Transform infra-red spectroscopy (FTIR) by using a FTIR spectrometer (model IFS-66v from Bruker) with a horizontal ZnS ATR accessory. The spectra were obtained at a resolution of 2 cm^{-1} and generally 200 scans were accumulated to provide a reasonable signal-to-noise ratio.

On the other hand, the aqueous stability of the DMSA-coated IONCa was evaluated by analyzing the size changes of the NPs upon incubation in HEPES buffer (pH 7.4) and DMEM culture medium supplemented with 10% fetal bovine serum (FBS) at 37 ºC under moderate stirring. The experiments were performed in triplicate. To do that, NP aliquots were taken, filtered (Triton free Millipore Millex, 1.2 μm porosity) into scattering cells and allowed to equilibrate at 37ºC for 30 min before recording changes in the size of drug-loaded micelles by DLS as described above.

2.5 *Cellular uptake by fluorescence microscopy*

DMSA-coated NP uptake was followed by bright field and/or fluorescence microscopy by seeding HeLa cells, MDA-MB-231 and mesenchemical stem cells (MSC) on poly-L-lysine coated glass coverslips (12×12 mm^2) placed inside 6-well plates (3 mL, $5 \cdot 10^4$ cells/well) and grown for 24 h at standard culture conditions (5% CO_2 at 37 ºC in Dulbecco's Modified Eagle Medium (DMEM) supplemented with 10% (v/v) FBS, 2 mM L-glutamine, 1% penicillin/streptomycin, 1 mM sodium pyruvate, and 0.1 mM MEM Non-Essential Amino Acids (NEAA)). Then, 50 μL of IONCs dispersions was added to cells. After 4 h of incubation cells were washed three times with PBS pH 7.4 and, then, fixed with paraformaldehyde 4% (w/v) for 10 min, washed with PBS, permeabilized with 0.2% (w/v) Triton X-100). The cells were

washed again with PBS, mounted on glass slides stained with ProLong® Gold antifade DAPI (Invitrogen) and cured for 24 h at -20 °C. Samples were visualized with 20X and 63X objectives using an inverted fluorescence microscope Leica DMI6000B (Leica Microsystems GmbH, Heidelberg Mannheim, Germany), whereby the blue channel corresponds to DAPI (λ_{ex} 355 nm), and the red channel to Bodipy Phalloidin (λ_{ex} 633 nm).

2.6 In vitro NP cytocompatibilty evaluation

Breast MDA-MB-231 and cervical HeLa cancer cells with an optical confluence of 80–90% were seeded into 96-well plates (100 µL, $1.5 \cdot 10^4$ cells/well) and grown for 24 h at standard culture conditions in 100 µL growth medium. After 24 h of incubation at 37 °C and 5% CO_2, IONCs solutions of different concentrations were added to cultured cells for cytocompatibility evaluation, and the cells subsequently incubated from 24 and 48 h. Cells exposed to NP-free culture medium were used as a negative control (100% viability) in both types of experiments. Cytotoxicity was evaluated at different time points using the CCK-8 proliferation assay. After incubation, 10 µL of CCK-8 reagent was added to each well, and after 2 h the absorption at 450 nm of cell samples was measured with an UV-Vis microplate absorbance reader (BioRad model 689, USA). Cell viability was calculated as:

$$\% \; viability = (Abs_{sample} / Abs_{control}) \times 100 \qquad (1)$$

where Abs_{sample} is the absorbance at 450 nm for cell culture samples with either bare copolymer solutions or drug formulations (free drugs and drug-loaded micelles), and $Abs_{control}$ for PBS controls. Assays were carried out in triplicate.

3. Results and discussion

3.1 Influence of reaction conditions and structural characterization of resulting NPs.

We have explored the synthesis of iron oxide NPs over a range of conditions based on an underlying one-pot reaction scheme that relies on the decomposition of a simple organometallic precursor of Fe, $Fe(acac)_3$, in a high-boiling organic solvent (dibenzyl ether) in the presence of a suitable surfactant as OA[13] with some modifications (see Materials and Methods section). The surfactant type and concentration affect the chemistry of the decomposition reaction and control nanocrystal nucleation and growth by reduction of the surface energy of the nanocrystal.[19] By subtle control of the reaction conditions, we can allow a size and shape-selective formation of different IONCs, in particular, nanocubes of different sizes but also truncated nanooctahedra and cubooctahedra. In a typical synthesis cubic Fe_3O_4 nanocrystals with a diameter of 48 ± 3 nm were obtained (see Materials and Methods section for details), as observed from TEM images (Figure 1a). They exhibited narrow size ditributions (<10%, criterion to consider a system as monodisperse), aspect ratios close to 1 and flat facets with only atomic steps. The crystalline structure of these cubic particles was revealed by high-resolution TEM (HRTEM) images (where the lattice fringes correspond to the Bravais lattice planes) selected area electron diffraction (SAED) and X-ray diffraction (XRD). A characteristic SAED pattern from a nanocube can be observed in Figure 1b, with typical reflections at (220), (311), (400) and (440). HRTEM further reveals that the {400} lattice fringes are parallel to the edges of the cube, while the {220} fringes run face-diagonally in the cube indicating that the cube-like particles are terminated with {100} planes (Figure 1c). The main direction <400> is indicated on the image. The

HRTEM analysis shows that these IONCs are single crystalline, {100}-bound cubes with an interplanar spacing of 2.9 and 2.1 Å, which is identified as the separation between the {220} and {400} planes, respectively, exclusive and consistent with the bulk values of magnetite with inverse spinel structure.[20]

From the fast Fourier transform (FFT) pattern of the same particle, we can conclude that the image can be indexed to the [001] zone axis of the spinel structure, since the cubes tend to deposit on flat faces of the [100] type (Figure 1c inset). Indexation of the spots was carried out on the basis of the file No. 85806 in ICSD, closely corresponding to magnetite (a = 8.399 Å; *Fd3m*; SG 227). Coincidence with maghemite is also possible. The cubical shape of the NCs is a result of a slower growth rate for the **{**100**}** facets as compared to all other facets.[21] The anisotropy of the growth rate can be attributed to a different adhesion of the stabilizer on the growing surface.

On the other hand, the X-ray diffraction pattern (Figure 1d) agrees with SAED and FFT of HRTEM images clearly, hence, confirming the spinel structure of magnetite with main diffraction peaks located at (111), (220), (311), (222) and (400) crystal planes arranged in a random fashion (the evaporation rate of the solvent was not controlled, hence, crystal superlattices are not formed). An inner contrast variation inside some nanocubes can also be observed, which might point to the existence of some core/shell NPs formed by the presence of an iron oxide matrix in which a metallic iron is embedded (either as a well-defined core or as small islands). However, the analysis of the magnetic properties seems to disregard a significant contribution of metallic iron, which can be explained by complete oxidation of certain particles during the washing procedure (carried out in air, precipitation by isopropanol and redispersion in pure solvent or magnetic separation of nanoparticles, in case of

octahedra).[20]

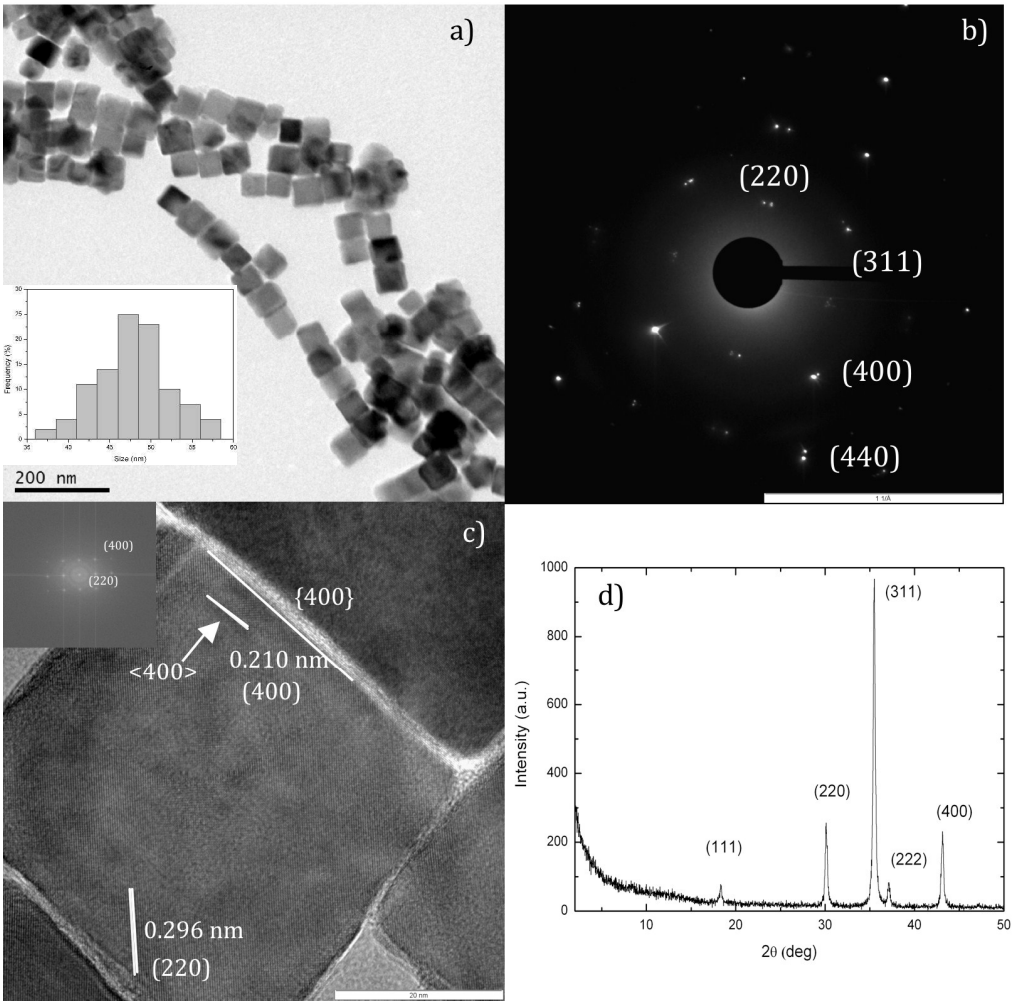

Figure 1: a) TEM image and b) SAED pattern of 48-nm IONCs. Inset in a) denotes the population size distribution. c) HRTEM image of the crystal planes of the synthesized nanocubes. In the inset, the FFT image can be observed. d) XRD of the synthesized IONCs.

In addition, the OA stabilizing layer can be directly observed from HRTEM images (Figure 1c) and its presence additionally corroborated by FTIR spectroscopy (Figure S1 in Supplementary Data): There exists a wide band at 3130–3630 cm^{-1} assigned to O–H vibrations; the sharp bands at 2923 and 2853 cm^{-1} assigned to the

asymmetric methyl stretching, and the asymmetric and symmetric methylene stretching modes, respectively; the characteristic bands at 1560 and 1443 cm^{-1} attributed to the asymmetric and symmetric COO^- stretches, which indicate that the OA chain is attached in a bidentate fashion with both oxygens symmetrically coordinated to the surface.[22] Finally, the Fe-O bonding is observed at ca. 545 cm^{-1}.

Cubic IONCs of different sizes could be obtained using the same procedure only by changing the concentration of organometallic precursor/volume of organic solvent, the heating ramp, the reaction temperature and time. For instance, by increasing the $Fe(acac)_3$ concentration from 1.4 to 2.6 mmol the size of nanocubes could be progressively increased from 27 ± 4 to ca. 94 ± 8 nm, respectively (Figure 2a-c). By increasing the reaction time from 39 to 60 and 90 min, the particles grew to a larger and more perfect cubic shape with edge dimensions of 58 ± 5 and 66 ± 5 nm, respectively (Figure 2e-f). Shorter reaction times (ca. 15 min) also allowed the formation of cubic IONCs with sizes of ca. 50 nm but these possessed less defined edges and were obtained in lower yields (ca. 65%) (Figure 2d). At this respect, it is possible to observe the presence of small NPs/magnetic material close to the surface of the cubic NPs as a consequence of the uncompleted reaction. The corresponding size distributions can be observed in Figure S2.

On the other hand, at lower reaction temperatures magnetic nanocubes were also formed but their size was slightly larger. For example, at a reaction temperature of 265 ºC cubic NPs with sizes of ca. 57 ± 7 nm and little larger polydispersity were obtained, with the reaction yield also lower (ca. 75%) as a result of the uncompleted decomposition of the iron precursor (Figure S3).[20]

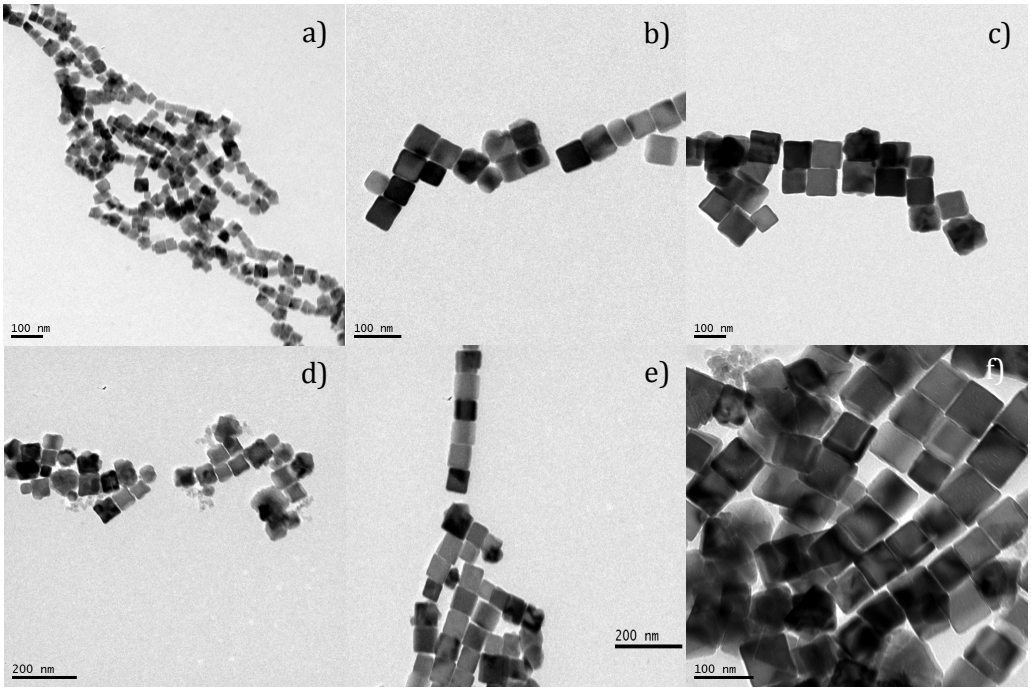

Figure 2: TEM images of iron oxide nanocubes obtained at different $Fe(acac)_3$ concentrations of a) 1.4 (27 nm), b) 2.1 (55 nm) and c) 2.6 mmol (94 nm); and at different reaction times ($[Fe(acac)_3]$ = 2.0) d) 15 min (50 nm), e) 60 min (58 nm), f) 90 min (65 nm).

The average dimensions of the cubic IONCs could be additionally controlled by varying the heating rate ramp. In particular, by successively increasing the heating ramp rate smaller particles with cubic morphology were gradually obtained, with lateral dimensions of 46 ± 4 nm, 39 ± 4 and 31 ± 5 nm at 7, 10 and 13 ºC/min, respectively (Figure 3a-c). Size distribution can be observed in Figure S4. A higher heating rate ramp produces a better nucleation step followed by the growth process. Nevertheless, further increases in the temperature ramp under our reaction conditions to 16 ºC/min led to the formation of slightly truncated octahedrical NPs (ca. 75% yield) (Figure 3d) with sizes of ca. 52 ± 5 nm. Some octahedrical NPs could be already observed at a heating rate of 13 ºC/min. The length between two opposite

vertices was taken as the particle size. These octahedral NPs could be formed thanks to the role played by OA as capping agent: At elevated heating rates OA molecules with negatively charged head groups can control the formation of densely packed {111} facets by selectively stabilizing the (111) planes (containing Fe^{2+} (or Fe^{3+}) cations only) because electrostatically the interaction with the charged {111} facets is favored in comparison to the uncharged {100} facets (containing Fe and O atoms). The polar (111) surface is energetically not stable. Goniakowski *et al*. pointed out that nature tends to avoid such a polarity catastrophe by changing the distribution of surface charges or the modification of the composition of the surface region. Detailed analysis of HRTEM images provided us with additional information about the structure and composition of these nanooctahedra, as shown in Figure 3e. The lattice spacings are measured at 0.488 nm, which corresponds to the {111} lattice planes of magnetite nanocrystsl, which is in agreement with the indexed FFT spot (see inset in Figure 3e). Therefore, the surface of nanooctahedra is delimitated by {111} crystallographic planes. We can also see some surface roughness, but the {111} facets are still maintained as the octahedrons' outer faces. The width of the spots might indicate the existence of defects or some type of nanostructured interior, in agreement with the contrast differences observed in the low magnification TEM images. Because TEM gives the two-dimensional (2D) projection of the objects, the octahedron-shape particles may look like hexagons, rectangles, or rhombi (Figure 3g-i).

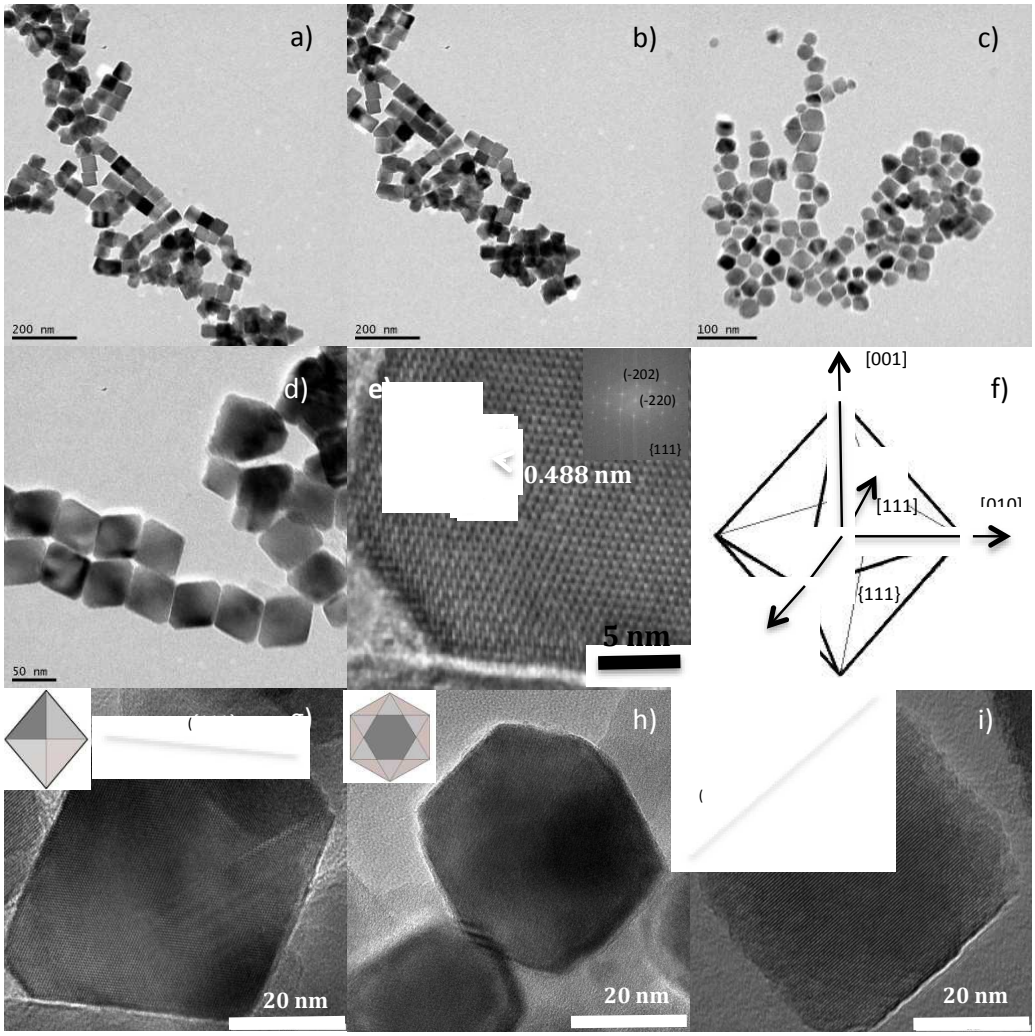

Figure 3: TEM images of nanocubes and nanooctahedra obtained after 30 min reaction upon heating ramps of a) 7, b) 10, c) 13, d) 16 ºC/min. e) HRTEM image of a truncated nanooctahedra displaying the characteristic interplanar distances. The inset shows the fast Fourier transform (FFT) of the displayed area. f) Schematic drawing of the octahedral shape of the nanocrystal in perspective, with indication of the main zone acis. HRTEM images showing slightly truncated octahedral particles observed under different zone axis as g) parallelogram, h) hexagonal, and i) rectangle. The insets show the schematic drawings of the octahedron projections.

Tunability of the particle size and shape could be also achieved by changing

the stabilizer/precursor molar ratio (see Figure 4 and Figure S5 for size distributions). In this way, at [OA]/[$Fe(acac)_3$] ratios (R) of 1.5, polyhedral NPs with sizes of ca. 46 ± 9 nm were obtained (Figure 4a). Upon raising to R = 1.75, cubic NPs are already formed with lateral mean sizes of ca. 63 ± 11 nm, although the size polydispersity is rather larger than at a molar ratio R = 2 typically employed in a routinary synthesis (Figure 4b). Cubic IONCs are also formed are observed at R = 2.5 and 3.5, respectively, with sizes ranging from 54 ± 7 nm to 66 ± 6 nm; meanwhile, at R = 4 cubooctahedral NPs with sizes of ca. 56 ± 8 nm are predominatly obtained, but some scarce cubic structures can be still observed (Figure 4c-e). At larger ratios (R = 5), the size of cubooctahedral NPs decreases to ca. 43 ± 6 nm whilst their yield is further increased (Figure 4f).

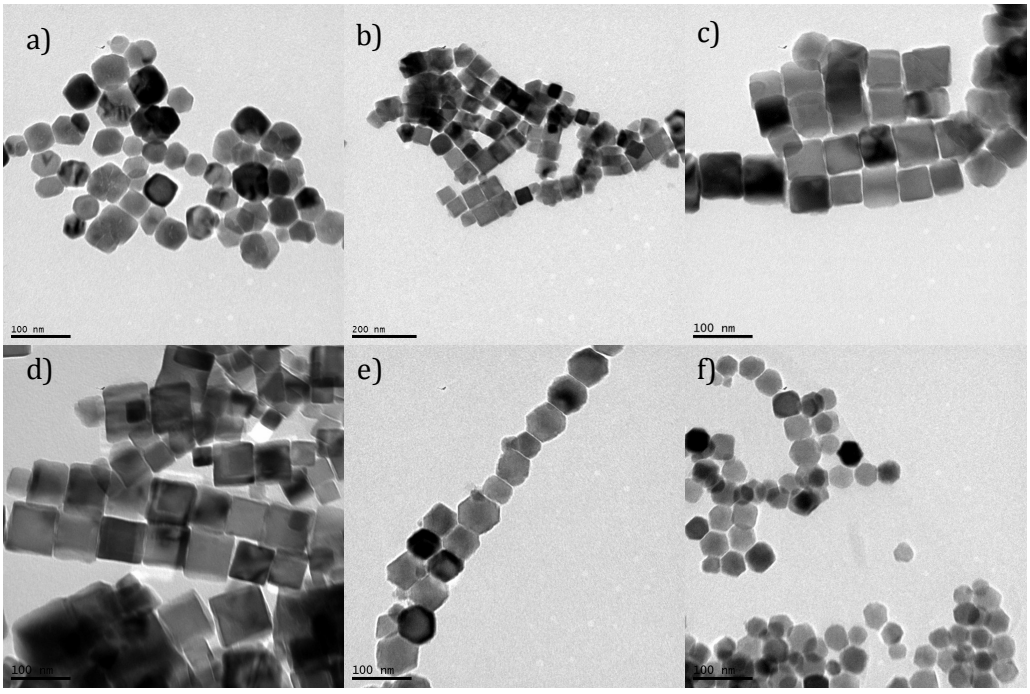

Figure 4: TEM images of magnetic NPs of different sizes and shapes by tuning the [OA]/[$Fe(acac)_3$] ratio, R: a) 1.5, b) 1.75, c) 2.5, d) 3.5; e) 4.0, f) 5.0.

3.2 Magnetic properties of iron oxide nanocrystals

Field- and temperature-dependent magnetic measurements were performed for different IONCs. Figure 5a-b shows the hysteresis loops recorded at 5 K and 300 K after zero-field cooling (ZFC) for 48 nm-magnetic nanocubes as an example. These particles display a soft antiferrimagnetic behavior even at low temperatures (5 K), with a coercive field $\mu_0 H_c$ of 46 mT, a remnant magnetization of 25 emu g^{-1}, and a high irreversibility field $\mu_0 H_{ir}$ of 0.4 T. $\mu_0 H_{ir}$ is the magnetic field at which both branches of the hysteresis loop merge into a single curve. Usually, high irreversibility fields can show that some of the nanoparticle spins have a "switching field", in the present case at 0.4 T, which may indicate the presence of a spin-glass-like, disordered magnetic phase that has been shown to exist at the surface of iron oxides and at the interfaces between Fe and iron oxide.[20] As the temperature raises, the field dependent magnetization shows hysteresis with lower coercive fields $\mu_0 H_c$, for example, 10 mT with an irreversibility field $\mu_0 H_{ir}$ of 0.2 T at 300K. The ratio of the remnant magnetization to the saturation magnetization is equal to ca. 0.25 at 5 K and 0.09 at 300 K. These low values for the remnant to high-field magnetization ratio may indicate the presence of superparamagnetic and/or paramagnetic phases.

The saturation magnetization, M_s, (determined by extrapolation of the magnetization *M(H)* to zero field, assuming that at high field region, $M(H) = M_s + \chi_d H^{23}$ and with χ_d being the high field susceptibility, which takes account of the surface spin disorder of the system) slightly decreases as temperature rises as coercitivities also do (Figure 5c). M_s values of these 48 nm-nanocube samples are slightly larger than those expected for bulk magnetite (M_s = 95 emu g^{-1}) for temperatures below 100 K, which in some cases arises from the presence of metallic iron inside the particles, as reported elsewhere.[15] Nevertheless, the relatively low H_c values denote a relatively low exchange anisotropy, which excludes the interaction at

ferromagnetic/ferrimagnetic interfaces present, for example, in metallic Fe core/oxidized Fe shell nanoparticles.[24] Hence, the large M_s values should stem from the reduced surface anisotropy of cubic IONCs since their surface spin state has the closest similarity with the core spin state.[17,25]

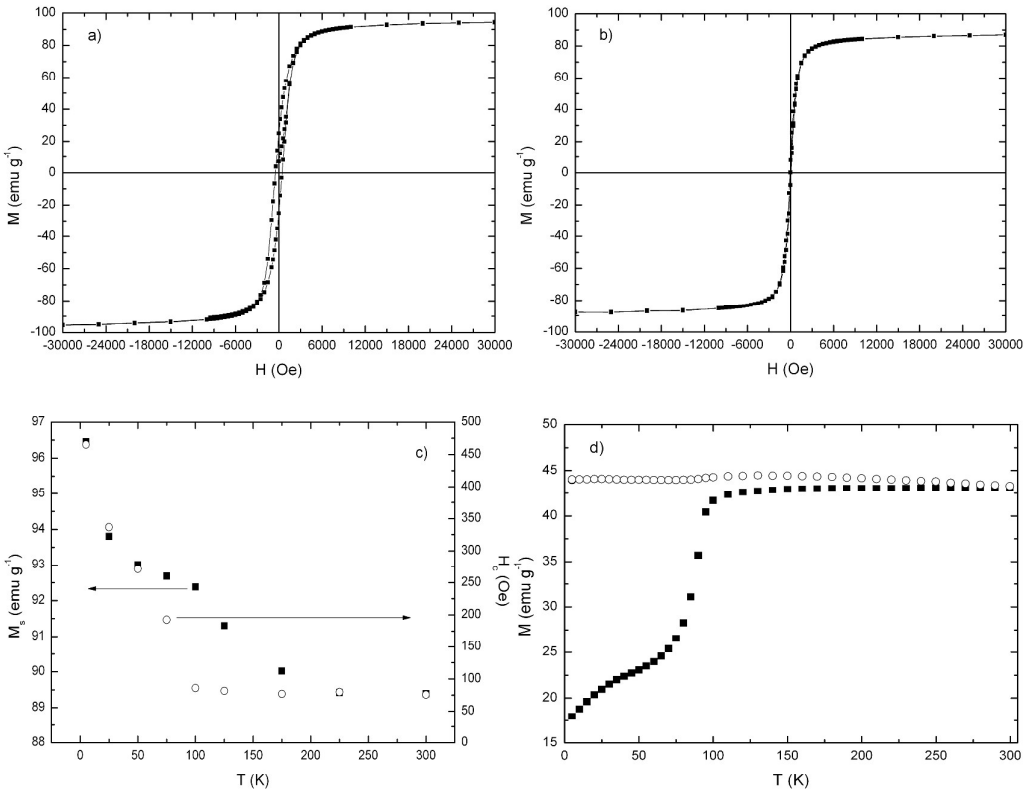

Figure 5: Magnetization as a function of the applied magnetic field for the powder 48 nm IONCs samples at a) 5 and b) 300 K. c) Temperature dependence of the saturation magnetization, M_S, and the coercive field, H_c. d) ZFC (■) and FC (○) curves of powder 48 nm IONCs samples.

Effective magnetic anisotropy energy density K_{eff} could be estimated from the temperature dependence of the coercive field (Figure 5c). A decrease in the coercivity with increasing temperature can be described theoretically for single-domain, non-interacting particles with a uniaxial magnetic anisotropy and randomly distributed

axis by

$$H_c(T) = H_{ci}\left(1 - \left(\frac{T}{T_{BL}}\right)^{2/3}\right) \quad (2)$$

where H_{ci} = 0.96 K_{eff} / ($M_s\rho$) is the intrinsic coercivity of the nanoparticle, ρ is the particle density, and T_{BL} is the blocking temperature of the nanoparticle assembly. K_{eff} = $4.6 \cdot 10^4$ J m^{-3} was determined from a fit with the temperature dependence of the coercivity field for 48 nm IONCs as an example very similar as that for bulk Fe (K_{eff} = $5 \cdot 10^4$ J m^{-3}). The ferromagnetic behavior of the present cubic NPs was further tested by temperature-dependent zero-field cooling (ZFC) and field cooling (FC) measurements (Figure 5d). From the ZFC-FC curve, we see no sign of superparamagnetic transition up to 300 K, which indicates that our NPs exhibit a relatively large anisotropy.[26]

Similarly to 48-nm nanocubes, antiferrimagnetic behavior was also observed for larger cubic IONCs (94 nm) in the whole measured temperature range. In contrast, for the smallest 27-nm nanocubes neither remanence nor coercivity was observed at 300 K indicating that these IONCs are in a superparamagnetic state with thermally unstable magnetization (Figure S6a-d). Moreover, the ZFC and FC thermomagnetic curves for these magnetic nanocubes confirm that upon increasing the temperature the ZFC magnetization increases and reaches a maximum. The blocking temperature, T_B, defined as the temperature at which the nanoparticle moments do not relax (are blocked) during the time scale of the measurement is found to be below room temperature (250 K) in contrast to what observed for larger nanocubes (see Figure 5e and Figure S6e). This suggests that nanocubes with a mean size of ca. 28 nm at room temperature are in the limit of the transition regime between superparamagnetism and ferrimagnetism.

The M_s values, determined by SQUID M-H curves at 5 K, does not show a very strong size dependence which stems mainly from the type of synthetic method: IONCs prepared by thermal decomposition show extremely high crystal quality, leading to size-independent, bulk-like magnetic and electronic properties. On the other hand, changes in M_s with size are also precluded because the portion of canted spins on the surface of the present NPs is very small in this size range.[12] Nevertheless, an initial M_s of 65 emu/g(Fe) for the 27 nm IONCs gradually increases to 97 emu/g(Fe) for the ca. 48 nm IONCs, that is roughly 110% of the bulk value (Figure 3b). This size dependent behavior of M_s can be attributed to the reduced surface contribution as the size of IONCs becomes large enough to be non-dissimilated from the bulk state, and the appearance of cation vacancies and surface spin canting on decreasing the particle size.[27] In addition, an increment of coercivity and remnant magnetization with size is also observed at the size regime of 27−94 nm for cubic NPs. For example, the remnant magnetization and coercivity of 27 nm nanocubes are ca. 16 emu g^{-1} and ca. 333 Oe at 5 K, much smaller than those values obtained for 94 nm IONCs, 31 emu g^{-1} and 609 Oe, respectively. Such increases have usually been attributed to a decreasing proportion of the pinned surface magnetic moments in overall magnetization as the nanocrystals grow in size. In our present case, as the particle size increases the coercivity at a given temperature increases rapidly upon the size exceeds the superparamagnetic limit, saturates when the size approaches the single-domain limit, and gradually decreases to the bulk value within the multidomain region.[28] Although the single-domain limit of 128 nm was estimated for Fe_3O_4 nanospheres,[29] our nanocubes did not show any sign of coercivity decrease up to ca. 100 nm. The shape anisotropy and the interaction between closely spaced nanocubes might be responsible for this increased critical size of the single domain particles.[30]

Nevertheless, a more rigorous investigation is being conducted to achieve a comprehensive understanding of the present results.

On the other hand, 52 nm octahedra and 56 nm cubooctahedra NPs showed slightly lower saturation magnetizations than cubic IONCs (for example, 91.8 and 89.9 emu/g at 5 K, respectively), but nanoctahedra still displaying ferromagnetic behavior in the whole temperature range analyzed (see Figure 6a-b and Figure S7), with coercivities of 382 and 52 Oe for octahedra and 215 and 39 Oe for cubooctahedra at 5 and 300 K, respectively. Moreover, the hysteresis loop recorded at 5 K for nanooctahedra has a certain narrowing at low fields and larger hysteresis at higher fields (see inset in Figure 6a). The low-field narrowing of the magnetic hysteresis might be observed in a sample comprising several ferromagnets with different anisotropy energies, but this is not the present case provided that these NPs are single cystals. Contribution from a superparamagnetic phase would also lead to the same effect. It should be noted that narrowing of the magnetic hysteresis is expected in the case of no exchange interaction between the magnetic particles. Otherwise, in a mixture of magnetically hard and magnetically soft phases a "exchange-spring"-like behavior would be observed. Because the particles in our sample are spatially separated by a surfactant, no significant exchange interaction is expected. Hence, nanocrystals with different shapes should demonstrate distinctly different coercivities that imply different surface pinning. The ZFC curve for octahedra increases as the temperature does, with a first shoulder at ca. 50 K and a maximum at 110 K. After such maximum there is a slight decrease in the magnetization values. The obtained T_B is ca. 325 K (Figure 6c). A similar profile is obtained for cubooctahedra, but with a less pronounced shoulder and a T_B of ca. 310 K (Figure S7c).

Finally, it is worth mentioning that from TEM pictures the formation of some aligned nanoparticles in the form of disordered unidimensional chains can be observed, specially for those with the cubic shape. The formation of such chain-like cubic aggregates would suggest the existence of relatively strong anisotropic dipolar forces mediating nanoparticle attachment; the face-to-face configuration in nanocubes would would allow for significantly more favorable chain formation than the case for spherical particles. Also, chains of cubic particles would have an axial magnetization as the lowest state in energy, while it is more unlikely to occur for spherical nanoparticles.

The chaining effect is particularly visible when drying the particle solution on the grids for TEM analysis. At least in this case, the dipolar forces become larger than the thermal energy and the van der Waals or electrostatic interactions,[31] and might have some influence on the magnetic properties of our samples. For example, squarer hysteresis loops for a magnetic field applied parallel to the direction of the alignment than for a magnetic field applied perpendicular to this direction would be expected as predicted by the Stoner-Wolhlfarth model, in agreement with our experimental ones.[32] Recent works have reported that coercivity, remanence and blocking temperature can either increase or decrease with an enhancement in the dipolar interactions depending on the ratio between the magnetostatic energy and the anistropy energy.[33] In particular, new experimental and simulation data have shown that for cubic nanoparticles forming one dimensional chains the area of the hysteresis loop and, hence, the coercitivity increases with the chain length and decreases with the separation between the chains.[32,34,35] We are currently analyzing in detail the influence on magnetic response of different types of ordered nanocube clusters, which will be the focus of a forthcoming publication.

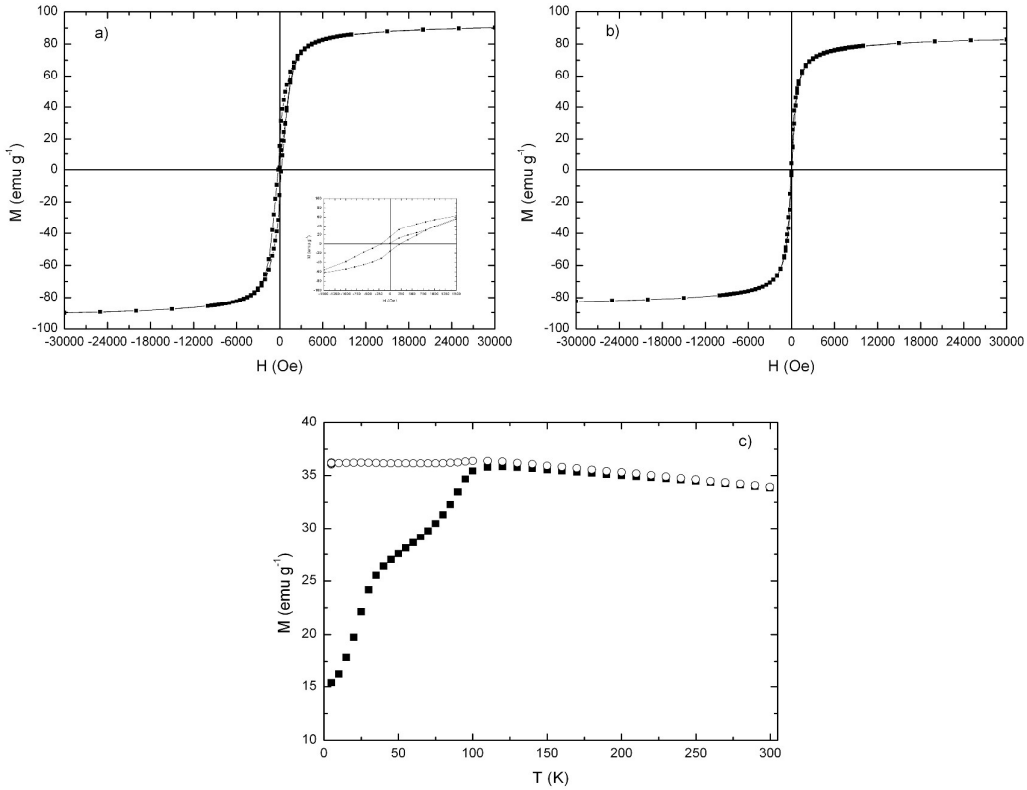

Figure 6: Magnetization as a function of the applied magnetic field for the powder 52 nm nanooctahedra samples at a) 5 and b) 300 K. c) ZFC (■) and FC (○) curves of powder nanooctahedra samples.

3.3. Preliminary stability and citotoxicity analysis of cubic IONCs.

The excellent magnetic properties of the synthesized magnetic NPs, specially those corresponding to cubic IONCs, make them interesting candidates to be used in biomedical applications as effective magnetic resonance imaging (MRI) contrast agents,[12,31.] heating probes in localized magnetic hyperthermia[5,16,36] and platforms/substrates for controlled and targeted delivery of bioactive compounds[37,38] Nevertheless, required conditions for the successful biomedical application of this type particles in biological complex media is their aqueous solubility and stability through functionalization with biocompatible molecules. Hence, firstly it is necessary

to provide the aqueous solubility to the synthesized NPs. As an example, 48 nm hydrophobic OA-coated cubic IONCs were able to be disperse in PBS buffer after coating with the bifunctional ligand dimercaptosuccinic acid (DMSA) through a solvent exchange process previously reported in literature.[39] This molecule is specially interesting since it provides free carboxylic and thiol groups at the nanoparticle surface that allow bonding different molecules and drugs though the formation of an amide bond. The successful modification of the NPs with DMSA was confirmed by FTIR spectroscopy (Figure S8). The size of the DMSA-coated NPs was ca. 100 nm and their surface electric charge ca. -42 mV over a wide range of pH (4-12), yielding very stable suspensions at pH 7.4. This negative charge was provided by the ionized carboxylate/and/or thiolate groups of the DMSA molecule not bonded to the cubic IONCs surface, and ensuring good colloidal stability through electrostatic repulsion and intraparticle disulfide bridging,[40] while providing free carboxylic groups for further functionalization.

To confirm the potential use in physiological environments, size-stabilities of DMSA-coated cubic IONCs as an example in different conditions were evaluated. As shown in Figure 7a, the initial size of DMSA-coated cubic IONCS in HEPES buffer at pH 7.4 is larger than that observed by TEM probably due to the formation of some NP clusters, as previously observed for spherical SPIONs after ligand exchange with DMSA.[39] In addition, size variations of the DMSA-coated NPs are negligible within 7 days; here, it is worth mentioning that HEPES was used instead than PBS since the latter contains phosphate ions which have been reported to have high affinity for the surface of iron oxide NPs displacing adsorbed molecules and resulting in loss of colloidal stability.[41] In contrast, NP sizes experienced an additional size variation after 1-day of incubation in DMEM medium supplemented with 10% FBS and, then, they

remain largely constant (Figure 7a). This observed increment is probably originated from protein adsorption onto the NP surface which the DMSA layer cannot completely avoid. In fact, analysis of the population size distributions under culture-cell conditions also allows to identify a second species with larger sizes appearing after short incubation with FBS probably corresponding to the formation of very few particle aggregates as a consequence of protein binding (Figure 7b). This population does not seem to increase either in size or number until the end of the time interval evaluated. Current studies in our group indicated that further functionalization, for example, with polymers such as polyethylene glycol (PEG) or polyoxazolines (POXAZ) and proteins such as human serum albumin (HSA) should avoid the appearance of such population due to the well-known ability of these (bio)polymers to avoid protein adsorption[42] while providing additional functionalities for coupling targeting moieties and/or bioactive agents to enhance cellular uptake, contrast imaging and/or therapeutical activity (manuscript in preparation).

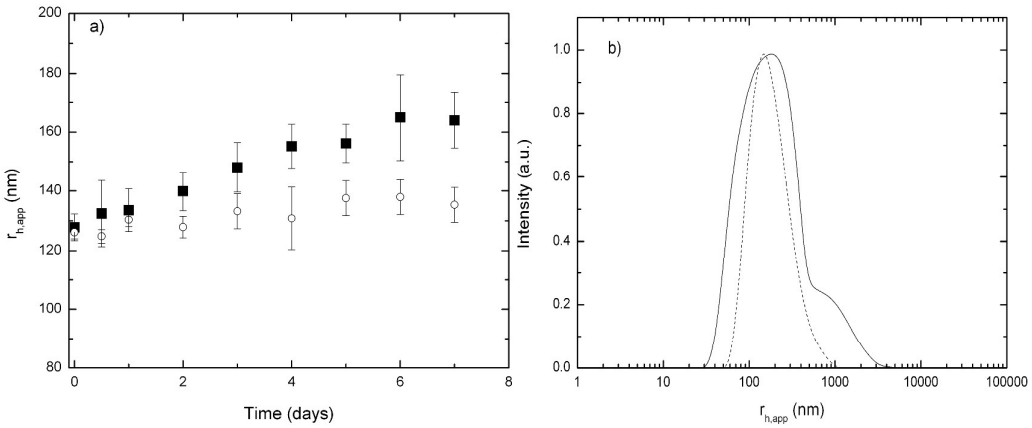

Figure 7: a) Size evolution with time of DMSA-coated IONCs in (○) HEPES buffer and (■) DMEM supplemented with 10 % FBS at 37 ºC. b) Population size distributions of DMSA-coated IONCs in HEPES (dashed line) and in culture medium (solid line) after 7 days of incubation.

On the other hand, preliminary cellular uptake and cytotoxicity experiments were performed in order to evaluate if the DMSA-coated cubic IONCs could be used as potential cores for developing multifunctional nanoplatforms. Here, it is worth reminding that the biological relevant entity upon particle administration would be the DMSA-coated NPs plus the protein layer adsorbed onto it. This involves certain changes in the surface charge and size of the NPs which very often are not considered while the physicochemical properties of nanoparticles affect their interactions with cells, uptake, internalization and final subcellular localization, depending on the cell type targeted and the nanoparticle surface charge, size and composition. In the present case, the DMSA-coated cubic IONCs in culture medium conditions possess a mean size of ca. 121 nm and a surface charge of ca. -27 mV, sufficient to provide colloidal stability, as commented previously.

Bright field and merged fluorescence microscopy images of DMSA-coated cubic IONCs incubated after 24 h confirms that the present NPs are relatively well-internalized inside different cell lines (cervical HeLa, breast MDA-MB-231 and mesenchemycal stem cells, MSC) and are observed to be located in the cytoplasm, with many of them showing a perinuclear distribution pattern (Figure 8a and Figure S9). Similar NP distribution is described for other nanoparticles in other tumor cell lines.[43] There exists also some NPs that could be considered to be inside the cellular nuclei; however, careful inspection through Z-stage monitoring confirms that these cubic IONCs are on top of the cells (not shown).

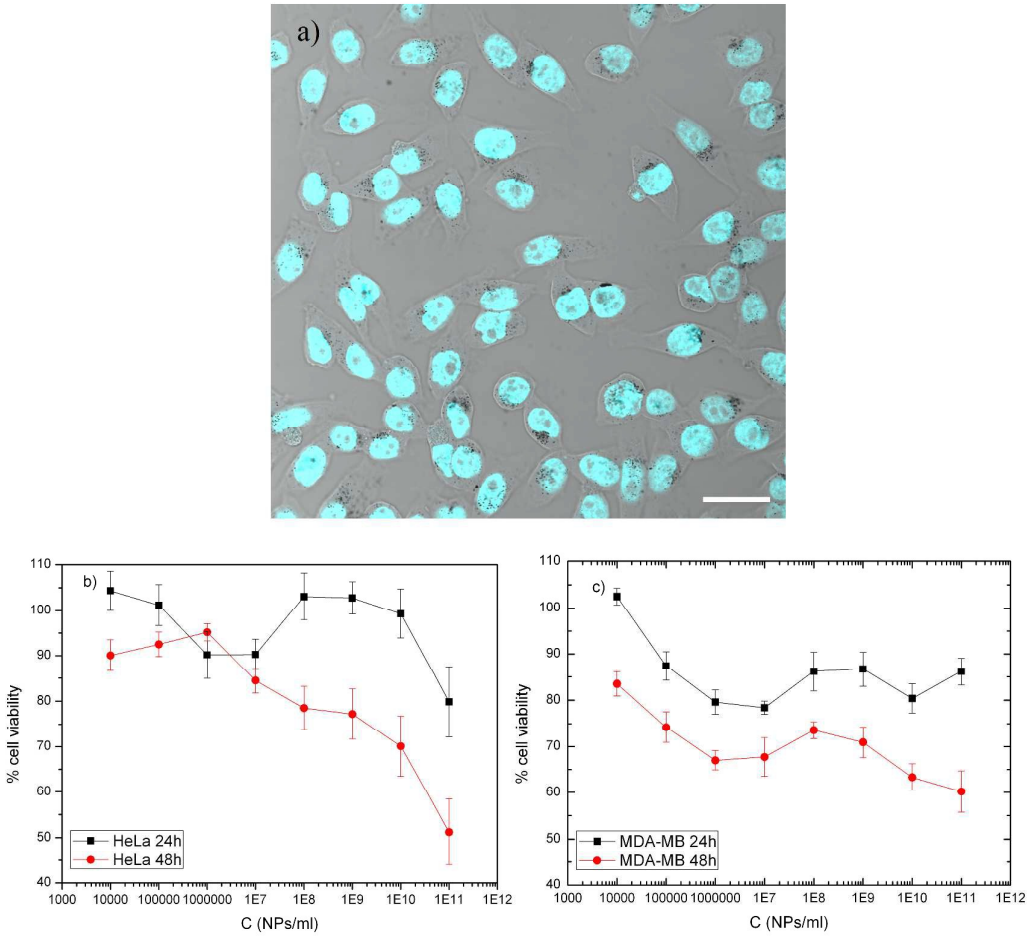

Figure 8: a) Merged bright field-fluorescence optical microscopy image showing the internalization and distribution of DMSA-coated cubic IONCs in HeLa cells as an example. Nuclei (in blue) were stained with DAPI. Cell viabilities after incubation with DMSA-coated cubic IONCs with b) HeLa and c) MDA-MB-231 cells after 24 and 48 h of incubation.

To study nanoparticle toxicity, we evaluated indirect and direct cytotoxic effects. Indirect cytotoxicity produces cytoarchitectural changes that impairs adhesion, differentiation, migration and cell division.[44-45] To analyze whether the presence of DMSA-coated cubic IONCs alters cytoskeletal components, we incubated HeLa cells alone or with NPs, followed by staining the cytoplasm with Bodipy-

phalloidin. We observed no differences in cycloskeletal organization between treated and control cells (Figure S10). Direct cytotoxicity includes alterations in cell metabolism, plasma or lysosomal membrane integrity, or mithocondrial metabolism.[46] These effects can decrease cell viability. Cell survival was analyzed using the CCK-8 assay (Figure 8b-c). Viability of cultured HeLa and MDA-MB-231 cells was slightly affected by DMSA-coated cubic IONCs, with cell mortalities slightly increasing from 0 to ca. 20% at NP concentrations among $1 \cdot 10^4$ and $1 \cdot 10^7$ NPs/mL, and remaining fairly constant up to $1 \cdot 10^{11}$ NPs/mL. Further incubation of IONCS-internalizing cells (48 h) led to an additonal decrease in cell viability of ca. 10-15% but still being above 70%, which is the thresold considerated for a nanodevice to be safe for biomedical applications. Also, it is worth mentioning that viabilities were lower for MDA-MB-231 cells if compared to HeLa ones, denoting the influence of cell phenotype in their sensitivity and biological response to the presence of nanomaterials. Current studies are being performed in order to analyze the mechansims of NP toxicity and degradation pathways of the present cubic IONCs inside cells.

4. Conclusions

We have discussed in this paper the effect of subtle changes in synthetic parameters on the formation of iron oxide nanocrystals though a modified high-temperature one pot decomposition method. It was found that highly monodisperse cubic iron oxide NPs of sizes ranging from 28 to 94 nm could be obtained by only changing the precursor concentration, the heating ramp rate or the reaction time. These cubes were observed to be single crystals enclosed by [100] flat faces. When using relatively high heating ramp rates (16 ºC/min) 52-nm truncated nanoctahedra enclosed by [111] facets; the detailed mechanism behind this shape change is not completely understood

but it might be to the establishment of favorable electrostatic interaction between polar (111) planes and the negativelly charged OA stabilizer molecules. Moreover, at high stabilizer/precursor molar ratios a shape transition from either cubic or octahedral NP to cubooctahedra takes place.

All obtained IONCs were observed to be ferrimagnetic in the whole temperature range analyzed, with blocking temperatures above room temperature. Moreover, saturation magnetization of cubic-shaped NPs of sizes above 40 nm was even larger than that of bulk magnetite, probably as a consequence of some metallic Fe irons in their crystal structure; however, if present, their concentrations should be small as confirmed by the relatively moderate values of the irreversible field (0.4 T). Moreover, a certain low-field narrowing of the magnetic hysteresis for truncated octahedra could be observed, which can derived by the absence of exchange interaction between NPs.

After a ligand exchange process cubic IONCs were coated with DMSA; this molecule imparted aqueous solubility and good colloidal stability in physiological conditions and provides chemical groups for further functionalization. Preliminary cellular internalization and toxicity demonstrated IONCs inside cells are arranged in a perinuclear distribution fashion, without altering either the structural or metabolic cellular state so that they can be considered safe and nontoxic even at very high concentrations, and prone to be used as cores for the development of more complex multifunctional nanoplatforms for combined imaging and therapy.

Acknowledgements

Authors thank Ministerio de Economía y Competitividad (MINECO) for research project MAT 2013-40971-R and Xunta de Galicia for projects EM 2013-046 and

GPC2015-007, respectively. S.B. greatly acknowledges MINECO for her Ramon y Cajal fellowship. A.P. and E.V.A. are grateful to MINECO for their FPU fellowships.

References

(1) S. K. Yen, P. Padmanabhan, S. T. Selvan, *Theranostics* 2013, **3**, 975-992.

(2) K. Turcheniuk, M. Khanal, A. Motorina, P. Subramanian, A. barras, V. Zaitsev, V. Kuncser, A. Leca, A. Martoriati, K. Cailliau, J. F. Bodart, R. Bouknherroub, S. Szunerits, *RSC Adv.* 2014, **4**, 865-875.

(3) M. Colombo, S. Carregal-Romero, M. F. Casula, L. Gutiérrez, M. P. Morales, I. B. Böhm, J. T. Heverhagen, D. Prosperi, W. J. Parak, *Chem. Soc. Rev.* 2012, **41**, 4306-4334.

(4) M. H. Cho, E. J. Lee, M. Son, J.-H. Lee, D. Yoo, J.-w. Kim, S. W. Park, J. S. Shin, J. Cheon, *Nat. Mater.* 2012, **11**, 1038-1043.

(5) R. Di Corato, A. Espinosa, L. Lartigue, M. Tharaud, S. Chat, T. Pellegrino, C. Ménager, F. Gazeau, C. Wilhelm, *Biomaterials* 2014, **35**, 6400-6411.

(6) R. Kappiyoor, M. Liangruska, R. Ganguly, I. K. Puri, *J. Appl. Phys.* 2010, **108**, 094702-094708.

(7) Q. A. Pankhurst, N. K. T. Thanh, S. K. Jones, J. Dobson, *J. Phys. D: Appl. Phys.* 2009, **4**, 193-201.

(8) P. Guardia, B. Batlle-Frugal, A. G. Roca, X. Batlle, *J. Magn. Magn. Mater.* 2007, **316**, e756-e759.

(9) D. A. Bazylinski, R. B. Frankel, *Nat. Rev. Microbiol*. 2004, **2**, 217-243.

(10) E. Alphandéry, S. Faure, L. Raison, E. Duguet, P. A. Howse, D. Bazylinski, *J. Phys. Chem. C* 2011, **115**, 18-22.

(11) D. Ling, N. Lee, T. Hyeon, *Acc. Chem. Res.* 2015, **48**, 1276-1285.

(12) N. Lee, Y. Choi, Y. Lee, M. Park, W. K. Moon, S. H. Choi, T. Hyeon, *Nano Lett.* 2012, **12**, 3127-3131.

(13) D. Kim, N. Lee, M. Park, B. H. Kim, K. An, T. Hyeon, *J. Am. Chem. Soc.* 2009, **131**, 454-455.

(14) S.-h. Noh, W. Na, J.-t. Jang, J.-H. Lee, E. J. Lee, S. H. Moon, Y. Lim, J.-S. Shin, J. Cheon, *Nano Lett.* 2012, **12**, 3716-3721.

(15) P. Guardia, J. Pérez-Juste, A. Labarta, X. Batlle, L. M. Liz-Marzán, *Chem. Commun.* 2010, **46**, 6108-6110.

(16) P. Guardia, R. Di Corato, L. Lartigue, C. Wihlem, A. Espinosa, M. garcía-Hernandez, F. Gazeau, L. Manna, T. Pellegrino, *ACS Nano* 2012, **6**, 3080-3091.

(17) Q. Song, Z. J. Zhang, *J. Am. Chem. Soc.* 2004, **126**, 6164-6168.

(18) M. V. Kovalenko, M. I. Bodnarchuk, R. T. Lechner, G. Hesser, F. Schäffler, W. Heiss, *J. Am. Chem. Soc.* 2007, **129**, 6352-6353.

(19) A. Shavel, B. Rodríguez-González, J. Pacifico, M. Spasova, M. Farle, L. M. Liz-Marzán, *Chem. Mater.* 2009, **21**, 1326-1332.

(20) A. Shavel, B. Rodríguez-González, M. Spasova, M. Farle, L. M. Liz-Marzán, *Adv. Func. Mater.* 2007, **17**, 3870-3876.

(21) Z. L. Wang, *J. Am. Chem. Soc.* 2000, **104**, 1153-1175.

(22) A. A. Khaleel, *Chem. Eur. J.* 2004, **10**, 925-932

(23) R. Grössinger, *Phys. Status Solidi A*, 1981, **66**, 665-674.

(24) J. Nogués, J. Sort, V. Langlais, V. Skumryev, S. Suriñach, J. S. Muñoz, M. D. Baró, *Phys. Rep.* 2005, **422**, 65-117.

(25) G. Salazar-Alvarez, J. Qin, V. Šepelák, I. Bergmann, M. Vasilakaki, K. N. Trohidou, J. D. Ardisson, W. A. A. Macedo, M. Mikhaylova, M. Muhammed, M. D. Baró, J. J. Nogués, J. J. Am. Chem. Soc. 2008, 130, 13234−13239.

(26) L.-M. Lacroix, N. F. Huls, D. Ho, X. Sun, K. Cheng, S. Sun, *Nano Lett.* 2011, **11**, 1641-1645.

(27) B. D. Cullity, Introduction to Magnetic Material; Addison-Wesley Publishing, Reading, MA, 1972.

(28) Modern Magnetic Materials: Principles and Applications; O'Handley, R. C., Ed.; Wiley-Interscience: New York, 1999.

(29) Nanoscale Materials in Chemistry; Klabunde, K. J., Ed.; Wiley-Interscience: New York, 2001.

(30) R. E. Dunin-Borkowski, M. R. McCartney, R. B. Frankel, D. A. Bazylinski, M. Posfai, P. R. Buseck, *Science* 1998, **282**, 1868-1870.

(31) H.- G. Liao, L. cui, S. Whitelam, H. Zheng, *Science* 2012, **336**, 1011-1014.

(32) E. Alphandéry, Y. Ding, A. T. Ngo, Z. L. wang, L. F. Wu, M. P. Pileni, *ACS Nano* 2009, **3**, 1539-1547.

(33) D. Farrel, Y. Cheng, R. W. McCallum, M. Sachan, S. A. Majetich, *J. Phys. Chem. B* 2005, **109**, 13409-13419

(34) C. Martínez-Boubeta, K. Simeonidis, A. Makridis, M. Angelakeris, O. Iglesias, P. Guardia, A. Cabot, L. Yedra, S. Estradé, F. Peiró, Z. Saghi, P. A. Midgley, I. Conde-Leborán, D. Serantes, D. Baldomir, *Sci. Rep.* 2013, **3**, 01652/1-01652/8.

(35) E. Alphandéry, A. T. Ngo, C. Lefévre, I. Lisiecki, L. F. Wu, M. P. Pileni, *J. Phys. Chem. C* 2008, **112**, 12304-12309.

(36) N. Lee, H. Kim, S. H. Choi, M. Park, D. Kim, H.-C. Kim, Y. Choi, S. Lin, B. H. Kim, H. S. Jung, H. Kim, K. S. Park, W. K. moon, T. Hyeon Proc. Natl Acad. Sci. USA 2011, **108**, 2662-2667.

(37) H. Kakwere, M. Pernia-Leal, M. E. Materia, A. Curcio, P. Guardia, D. Niculaes, R. Marotta, A. Falqui, T. Pellgrino *ACS Appl.* Mater. Interfaces 2015, **7**, 10132-

10145.

(38) Y. Wang, N. L. Inbrahim, J. Jiang, S. Gao, N. Erathodiyil, J. Y. Ying. *J. Control. Release* 2013, **169**, 211-219.

(39) L. I. Cabrera, A. Somoza, J. F. Marco, C. J. Serna, M. Puerto-Morales. *J. Nanopart. Res.* 2012, **14**, 873/1-873/14.

(40) A. Ruiz, P. C. Morais, R. Bentes de Azevedo, Z. G. M. Lacava, A. Villanueva, M. P. Morales. *J. Nanopat. Res*. 2014, **16**, 2589/1-2589/20.

(41) A. López-Cruz, C. Barrera, V. L. CaleroDdelC, C. Rinaldi. *J. Mater. Chem*. 2009, **19**, 6870-6876.

(42) T. A. Larson, P. P. Joshi, K. Sokolov. *ACS Nano 2012*, **6**, 9182-9190.

(43) A. Villanueva, M. Canete, A. G. Roca, M. Calero, S. Veintemillas-Verdaguer, C. J. Serna, M. P. Morales, R. Miranda. *Nanotechnology* 2009, **20**, 115103.

(44) A. M. Lipski, C. J. Pino, F. R. Haselton, I. W. Chen, V. P. Shastri. *Biomaterials* 2008, **29**, 3836-3846.

(45) N. Perdonet, X. Fang, Y. Sun, A. Bakhtina, A. Ramakrishnan, J. Sokolov, A. Ulmann, M. Rafaloivich. *Small* 2006, **7**, 766-773.

(46) S. A. Altman, L. Randers, G. Rao. *Biotechnol. Prog*. 1993, **9**, 671-674.

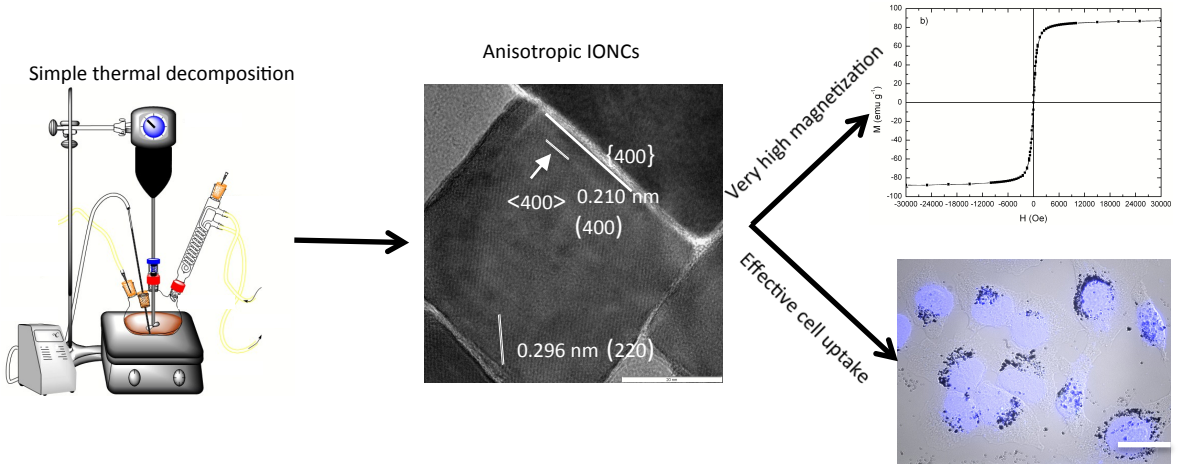

Monodisperse non-spherical magnetic obtained by simple methods display excellent magnetic properties with high potential for theranostic applications